AGU PUBLICATIONS

JGR

Journal of Geophysical Research: Solid Earth

RESEARCH ARTICLE

10.1002/2015JB011983

Key Points:
- Study of the evolution of pore fluid pressure during laboratory stick slip
- Effect of hydrological boundary conditions on recurrence time of stick slip
- Conceptual model for granular fault gouge deformation

Supporting Information:
- Figures S1–S3

Correspondence to:
M. M. Scuderi,
marco.scuderi@uniroma1.it

Citation:
Scuderi, M. M., B. M. Carpenter, P. A. Johnson, and C. Marone (2015), Poromechanics of stick-slip frictional sliding and strength recovery on tectonic faults, *J. Geophys. Res. Solid Earth*, *120*, doi:10.1002/2015JB011983.

Received 25 FEB 2015
Accepted 23 SEP 2015
Accepted article online 29 SEP 2015

Poromechanics of stick-slip frictional sliding and strength recovery on tectonic faults

Marco M. Scuderi[1,2], Brett M. Carpenter[3], Paul A. Johnson[4], and Chris Marone[1,2,3]

[1]Department of Geosciences, Pennsylvania State University, State College, Pennsylvania, USA, [2]Dipartimento di Scienze della Terra, La Sapienza University of Rome, Rome, Italy, [3]Istituto Nazionale di Geofisica e Vulcanologia, Rome, Italy, [4]Geophysics Group, Los Alamos National Laboratory, Los Alamos, New Mexico, USA

Abstract Pore fluids influence many aspects of tectonic faulting including frictional strength aseismic creep and effective stress during the seismic cycle. However, the role of pore fluid pressure during earthquake nucleation and dynamic rupture remains poorly understood. Here we report on the evolution of pore fluid pressure and porosity during laboratory stick-slip events as an analog for the seismic cycle. We sheared layers of simulated fault gouge consisting of glass beads in a double-direct shear configuration under true triaxial stresses using drained and undrained fluid conditions and effective normal stress of 5–10 MPa. Shear stress was applied via a constant displacement rate, which we varied in velocity step tests from 0.1 to 30 μm/s. We observe net pore pressure increases, or compaction, during dynamic failure and pore pressure decreases, or dilation, during the interseismic period, depending on fluid boundary conditions. In some cases, a brief period of dilation is attendant with the onset of dynamic stick slip. Our data show that time-dependent strengthening and dynamic stress drop increase with effective normal stress and vary with fluid conditions. For undrained conditions, dilation and preseismic slip are directly related to pore fluid depressurization; they increase with effective normal stress and recurrence time. Microstructural observations confirm the role of water-activated contact growth and shear-driven elastoplastic processes at grain junctions. Our results indicate that physicochemical processes acting at grain junctions together with fluid pressure changes dictate stick-slip stress drop and interseismic creep rates and thus play a key role in earthquake nucleation and rupture propagation.

1. Introduction

The pore fluid pressure acting within fault rock and fault gouge has an important influence on the mechanical strength of crustal fault zones, via a variety of interconnected mechanical and chemical processes. The shear strength of a fault zone (τ_f) can be described as

$$\tau_f = \mu(\sigma_n - P_p). \quad (1)$$

where μ is the coefficient of friction, σ_n is the applied normal stress, and P_p is the pore fluid pressure acting within the pore space, which modulates the effective normal stress (σ'_n) [*Hubbert and Rubey*, 1959]:

$$\sigma'_n = \sigma_n - P_p \quad (2)$$

Equation (2) indicates that variations in the pore fluid pressure have a direct influence on the effective normal stress and thus on fault strength. Several models have been proposed for the mechanical effect of P_p on fault strength during the seismic cycle. The fault-valve model [*Sibson*, 1981, 1982] indicates that frictional strength and slip stability, on a hydraulically isolated fault (i.e., undrained conditions), can be controlled by fluctuations in P_p, which may arise directly from compaction during the interseismic stage of the seismic cycle [e.g., *Sleep and Blanpied*, 1992]. Alternatively, shear-driven dilatancy can cause pore fluid depressurization, increasing the effective normal stress and thus resulting in dilatancy hardening [e.g., *Rudnicki and Rice*, 1975; *Rudnicki*, 1984; *Segall et al.*, 2010; *Samuelson et al.*, 2011; *Segall and Lu*, 2015]. Moreover, shear heating during dynamic rupture can increase pore fluid pressure and thus decrease fault strength [e.g., *Andrews*, 2002; *Bizzarri and Cocco*, 2006; *Segall and Rice*, 2006; *Garagash and Germanovich*, 2012].

In fault gouge, time- and slip-dependent asperity contact processes can alter frictional resistance, via increasing the quantity and/or quality of the contacts [e.g., *Hickman and Evans*, 1992; *Hickman et al.*, 1995; *Dieterich and Kilgore*, 1994; *Frye and Marone*, 2002; *Rossi et al.*, 2007; *Li et al.*, 2011; *Renard et al.*, 2012]. Time-dependent chemical reactions, such as pressure solution at highly stressed grain contacts can play an important role in

controlling the long-term shear strength along faults, by promoting aseismic slip (i.e., creep) and leading to variations in time-dependent strengthening between earthquakes [*Chester and Higgs*, 1992; *Hickman et al.*, 1995; *Bos and Spiers*, 2002; *Niemeijer et al.*, 2010; *Verberne et al.*, 2013]. However, the effects of the interaction between the granular matrix and fluids on the mechanics of brittle faulting are still poorly understood. For a tectonic fault zone, the evolution of shear strength, during the interseismic stage of the seismic cycle, is partially controlled by the pore fluid pressure and the state of drainage [e.g., *Samuelson et al.*, 2011].

Hydraulically isolated faults (i.e., undrained) are thought to be representative of many natural fault zones worldwide that host major earthquakes [e.g., *Sibson*, 1992; *Kitajima and Saffer*, 2012; *Hirono and Hamada*, 2010; *Hasegawa et al.*, 2011]. Field and seismological observations also suggest that anomalous (i.e., near lithostatic) pore fluid pressures are present at the base of the seismogenic zone [e.g., *Sibson*, 1992; *Audet et al.*, 2009]. In this context, understanding how the pore fluid pressure evolves during the inter-seismic stage of the seismic cycle, on undrained faults, is of primary importance because pore fluid pressure can control the onset of dynamic instability, and recurrence of major earthquakes, and thus have important implications for models of earthquake prediction [*Chester*, 1995; *Rubinstein et al.*, 2012a].

Numerous experimental and theoretical works have been conducted to characterize the micromechanics of deformation within fluid-filled granular media [e.g., *Samuelson et al.*, 2011; *Goren et al.*, 2011]. In laboratory experiments, a common feature during the "stick" phase, preceding dynamic instability ("slip"), is premonitory slip, and such aseismic creep may cause compaction or dilation depending on the initial porosity and other conditions [e.g., *Anthony and Marone*, 2005]. Interseismic creep compaction would tend to increase pore fluid pressure and reduce fault strength causing failure. The creep-slip model proposed by *Beeler et al.* [2001a] shows that in order to model the small repeating earthquake sequence at Parkfield, a relatively large amount of aseismic creep during the interseismic period is needed. However, the mechanical processes that control creep and the evolution of stress within fault zones during the creeping stage of faulting are still poorly understood. To our knowledge, only a few laboratory experiments have been performed within a stick-slip frictional sliding regime under undrained boundary conditions [*Sundaram et al.*, 1976; *Teufel*, 1980]. They showed that coincident with the onset of premonitory slip, the pore fluid pressure decreases due to dilation. *Teufel* [1980] observed contact-induced extension fractures developing from high stress concentrations at asperity contacts and interpreted that as a mechanism for pore pressure reduction during premonitory slip. However, both of these studies were performed on bare rock surfaces in direct contact, without the presence of granular fault gouge.

The aim of this paper is to explore the feedback processes between micromechanical deformation at grain contacts and the evolution of pore fluid pressure during the full stick-slip cycle of frictional sliding. We focus on the roles that shear-induced dilatancy and pore fluid depressurization have on aseismic creep, stress drop magnitude, and recurrence time for a hydraulically isolated experimental fault.

2. Experimental Methods

We performed double-direct shear experiments in a biaxial deformation apparatus equipped with a pressure vessel to allow a true-triaxial stress field (Figure 1). A fast acting servo-hydraulic system was used to control applied stresses and/or displacements. The applied fault normal stress was maintained constant via a load-feedback servo control loop. Similarly, shear stress was applied via a controlled shear displacement rate imposed at the fault boundaries using servocontrol. Forces were measured using custom-built, beryllium-copper, strain gauged load cells with an amplified output of ±5 V and an accuracy of ±0.01 kN, which is calibrated regularly with a device traceable to National Institute of Standards and Technology. Displacements were measured via direct current displacement transducers, with an accuracy of ±0.1 μm and positioned between the moving ram and the fixed biaxial frame (Figure 1). A linear variable differential transformer (LVDT) accurate to ±0.1 μm was positioned inside the pressure vessel, across the gouge layers, to more accurately measure fault compaction and dilation and to avoid artifacts of piston friction associated with measurements made external to the pressure vessel (Figure 2). Load point displacement measurements are corrected for the stiffness of the testing apparatus, with nominal values of 0.5 kN/μm for the vertical frame and 0.4 kN/μm for the horizontal frame.

The pressure vessel is accessed via removable doors and dynamic O-rings allow the vertical and horizontal ram to reach the sample (Figure 1) (see *Samuelson et al.* [2009] for details). Fluid ports allow application of

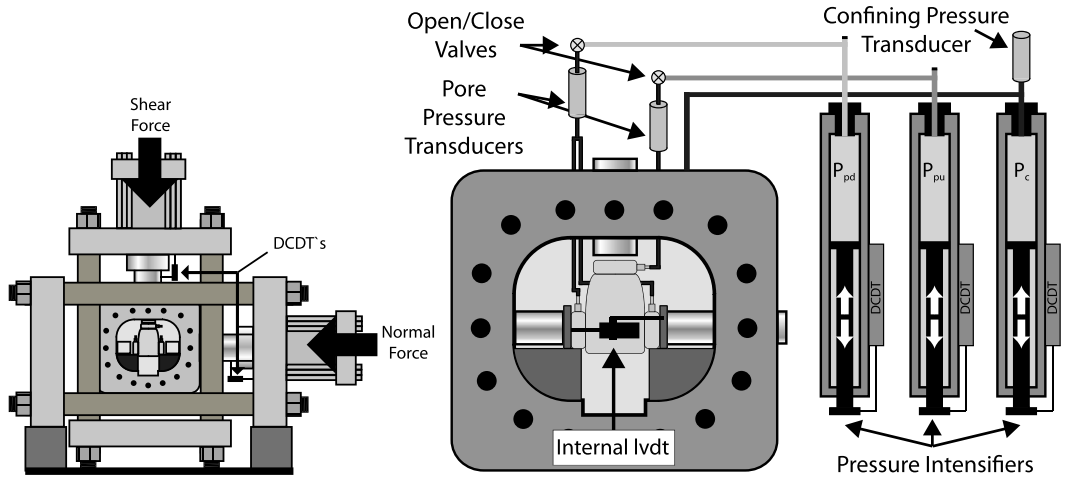

Figure 1. (a) Schematic representation of the biaxial deformation apparatus and pressure vessel. (b) Experimental configuration, showing the sample assembly placed within the triaxial pressure vessel. A high resolution LVDT is fixed across the sample assembly in the pressure vessel. Represented on the right are the pressure intensifiers used to apply confining pressure (P_c), up-stream (P_{pu}), and down-stream (P_{pd}) fluid pressure.

up- and down-stream pore fluid pressure (P_{pa} and P_{pb}, respectively) to the fault zone (Figure 1). Pore fluid and confining pressure are servo-controlled using fast-acting hydraulic servocontrollers. Confining pressure is applied using a hydrogenated, paraffinic white oil (XCELTHERM 600, Radco Industries) and maintained constant throughout drained tests using a load-feedback control mode. For pore fluid we used deaerated water (Nold Deaerator S-530) and monitored pressure with diaphragm pressure transducers accurate to ±7 kPa (Figure 1). In order to achieve fully undrained boundary conditions and accurately measure variations

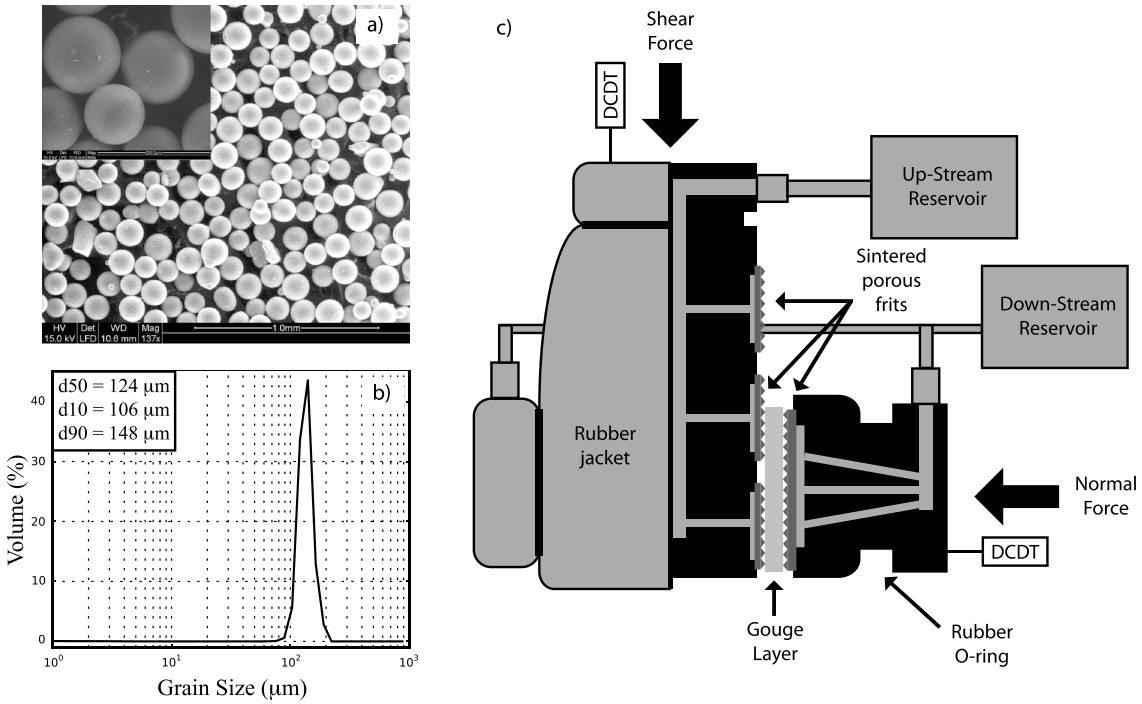

Figure 2. Starting material and experimental sample assembly. (a) SEM image of undeformed glass beads. Inset shows a zoom of the grains. (b) Particle size distribution data. (c) Sample assembly for double-direct shear configuration. In black, forcing blocks equipped with conduits for fluid flow (light gray). The two side blocks are connected to a down-stream fluid reservoir and the central block to an up-stream fluid reservoir. Sintered porous frits, positioned in depressions within the forcing blocks, are used to homogenously distribute fluids within the gouge layers.

Table 1. Experimental Details[a]

Experiment	Drainage State	σ'_n (MPa)	σ_n (MPa)	P_c (MPa)	P_p (MPa)	V_L (μm/s)
p3643	Undrained	5	5.153	2.5	1.5	1-3-10-30
p3767						
p3847						
p4222	Undrained	5	5.153	2.5	1.5	0.1-1
p3883	Drained	5	5.153	2.5	1.5	1-3-10-30
p3949						
p4001						
p3644	Undrained	10	11.76	6	5	1-3-10-30
p3768						
p3848						
p4223	Undrained	10	11.76	6	5	0.1-1
p3884	Drained	10	11.76	6	5	1-3-10-30
p3946						
p4002						

[a]All experiments were run using an initial layer thickness of 5 mm. Reported are the values of normal stress (σ_n), confining pressure (P_c), and pore fluid pressure (P_p), combined to obtain an effective normal stress (σ'_n).

in pore fluid pressure, pore pressure transducers were positioned very close to the samples, at the top of the pressure vessel and isolated from the intensifiers via mechanical valves (Figure 1). Data were recorded using a 24-bit ±10 V, 16-channel simultaneous analog-to-digital converter at a rate of 10 kHz, which was then averaged to obtain sampling rates between 1 Hz and 10 kHz.

2.1. Starting Material and Sample Preparation

We sheared layers of granular fault gouge in a double direct shear configuration (Figure 2). Gouge layers were composed of smooth, soda-lime glass beads (GL-0191) purchased from Mo-Sci, Rolla, Missouri (Figure 2a). Chemical composition (by weight) was silica 65–75%, sodium oxide 10–20%, calcium oxide 6–15%, magnesium oxide 1–5%, and aluminum oxide 0–5%. Particle size analysis shows a median diameter (d50), by mass, of 124 μm with a range of diameters from 90 to 150 μm (Figure 2b). Glass beads have been widely used in previous works as they share key characteristics with rock [*Weeks et al.*, 1991] and exhibit highly reproducible stick-slip frictional sliding under geophysical stresses [*Mair et al.*, 2002; *Savage and Marone*, 2007, 2008; *Johnson et al.*, 2008, 2013; *Leeman et al.*, 2014]. A second advantage of uniform granular beads is that they allow simple, accurate post experiment analysis of changes in grain morphology [*Rossi et al.*, 2007; *Scuderi et al.*, 2014]. Finally, spherical beads are commonly used in numerical simulations, which is the focus of ongoing work [e.g., *Ferdowsi et al.*, 2014a, 2014b].

The double-direct shear configuration under true-triaxial stresses consists of a three-block assembly, with a central forcing block and two stationary side blocks (Figure 2c). Forcing blocks are equipped with high-pressure fittings and internal conduits and channels that provide fluid access to the granular layer via sintered, stainless steel porous frits with permeability k~10^{-11} m^2, in contrast to the permeability of the gouge layers, which are characterized by an initial porosity of ~40% and k~10^{-12} m^2. The frits are press fit into the forcing blocks and used to homogenously distribute fluids to the gouge layer boundaries (Figure 2c). Frits were machined with grooves using an EDM (electronic distance measurement) technique to avoid damaging the pore structure; grooves are 0.8 mm in height with 1 mm spacing and oriented perpendicular to the shear direction to ensure that shear occurs within the gouge layers and not at the layer boundaries [e.g., *Anthony and Marone*, 2005]. The nominal frictional contact area is 5.4 cm × 6.2 cm, and we refer all measurements of stress, displacement, and fluid volume and pressure changes to one layer. For these sample dimensions and loading configuration, normal stress on the friction layers is determined by applied stress σ_n and confining pressure P_c as $\sigma_n + 0.539\ P_c$, where the prefactor for P_c represents a geometric effect in the force balance [*Samuelson et al.*, 2009].

Gouge layers were prepared using a precision leveling jig in order to produce uniform and reproducible layer thicknesses of 5 mm. Once the layers were prepared, and the side forcing blocks secured to the central block, the assembly (gouge layers + forcing blocks) was sealed with a flexible latex jacket in order to isolate the sample from the confining medium [*Samuelson et al.*, 2009; *Scuderi et al.*, 2013]. Tubing for fluid access was then connected, and the sample assembly placed in the pressure vessel (Figure 1).

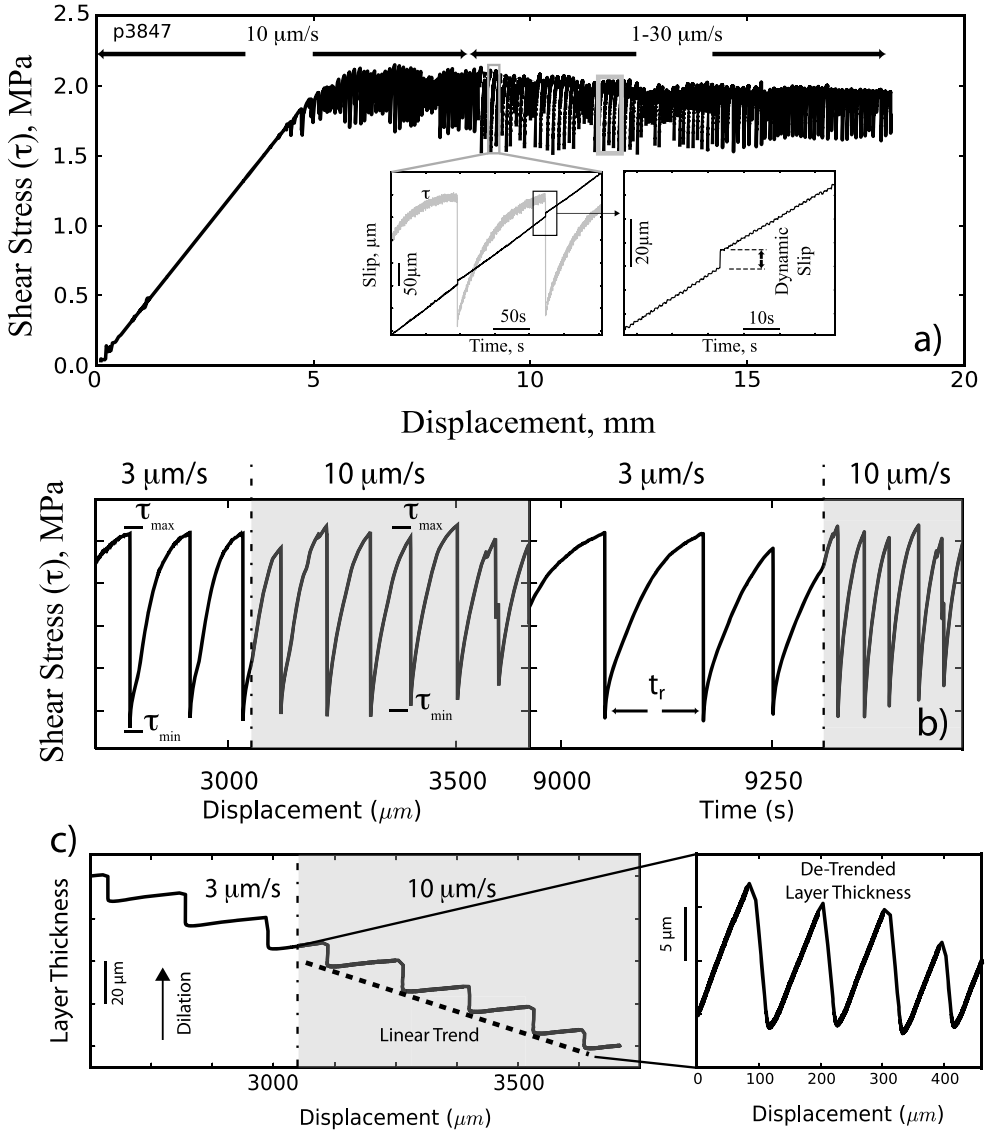

Figure 3. (a) Representative curve for a typical experiment showing shear stress as a function of shear displacement. (b) Details of stick-slip evolution across a velocity step from 3 to 10 μm/s (gray box in Figure 3a). Left-hand side shows stress drop ($\Delta\tau = \tau_{max} - \tau_{min}$) decreasing upon a velocity increase. Right-hand side shows a sudden decrease in event recurrence time (t_r) upon the same velocity step. (c) Evolution of gouge layer thickness with shear displacement. Left-hand side shows raw data for the same section of the experiment shown in Figure 3b. Right-hand side shows data for the 10 μm/s section once the linear trend for geometrical layer thinning, due to experimental geometry, is removed.

2.2. Experimental Procedure

Experiments were conducted at effective normal stresses ($\sigma'_n = \sigma_n + (0.539\ P_c) - P_p$) of 5 and 10 MPa, under drained and undrained boundary conditions (Table 1). Values of effective normal stress were chosen to be well within the nonfracture regime for glass beads (5 MPa) and near its upper limit (10 MPa) [e.g., *Mair et al.*, 2002; *Anthony and Marone*, 2005]. Each experiment started by applying a small normal force to the sample until the layers were fully compacted. We then made an accurate measurement of the layer thickness in situ, from which high-resolution measurements of changes in layer thickness are referred. At this point the pressure vessel was closed, filled with oil, and a small confining pressure of 2 MPa was applied. An up-stream pore pressure (P_{pa}) of 1 MPa was applied, while the down-stream side (P_{pb}) was left open to the atmosphere, until flow through the layers was established. A vacuum pump was then connected to the P_{pb} line, in order to further remove residual air within the pore space. Once we ensured

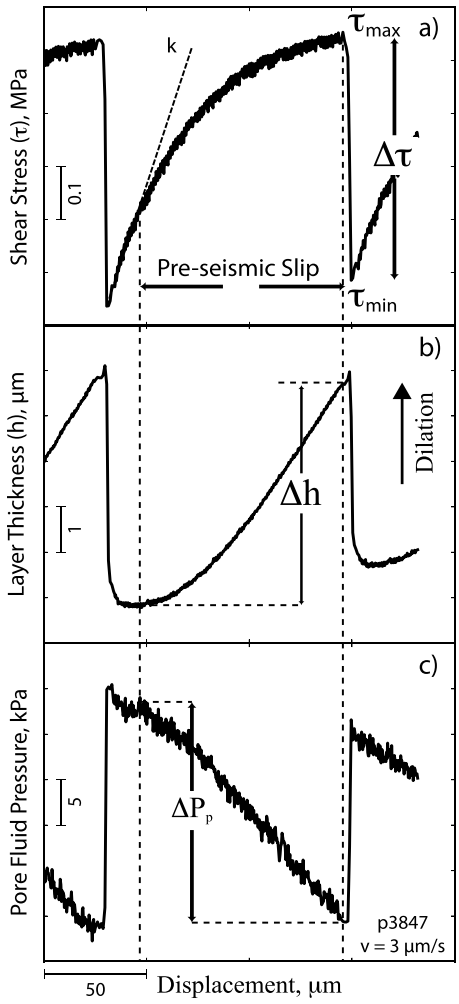

Figure 4. Details for a typical stick-slip event. (a) Evolution of shear stress with displacement. Stress builds up linearly during elastic loading characterized by stiffness of k. Deviation from elastic loading marks the onset of preseismic slip and creep, until a maximum stress is reached (τ_{max}). Parameter $\Delta\tau$ represents the dynamic stress drop during coseismic slip. (b) Relative evolution of granular gouge layer thickness. Dilation during preseismic slip is followed by abrupt compaction corresponding with dynamic slip. (c) Pore fluid pressure decreases during preseismic slip (i.e., effective normal stress increases due to depressurization), followed by an abrupt increase during dynamic stress drop.

that gouge layers were fully saturated, the down-stream pore pressure line was connected to the pressure intensifier (Figure 1) at 1 MPa and the system left to equilibrate. Stresses (σ_n, P_c, and P_p in this order) were subsequently increased to the target values of effective normal stress, 5 or 10 MPa. At this stage, for undrained boundary conditions (i.e., constant pore fluid volume), we closed both pore fluid valves just beyond the pressure transducers (Figure 1). In these experiments we measure variations in pore fluid pressure during shearing. For experiments under drained boundary conditions, the valves were left open and water was free to move to and from the sample. Leak tests were performed on the system (intensifiers + pore pressure lines), regularly, and revealed maximum leak rates of $<1\times10^{-6}$ cm^3/s for P_{pa} and $<1.4\times10^{-4}$ cm^3/s from P_{pb}. Leaks were linear in time, and data were corrected accordingly.

Layers were subject to shear loading by driving the center block of the double direct shear assembly at constant rates (Figure 2). As shear stress first began to increase the sample jacket and rubber sheets that extend under the side forcing blocks flatten. We account for this elastic compaction via an elastic correction. At the end of each experiment the sample was carefully removed from the pressure vessel, the jacket removed, and material (~2 g) from the central shear zone of the gouge layers was collected for visual and microstructural analysis via a scanning electron microscope (SEM). For a given boundary condition (i.e., drained/undrained at 5 and 10 MPa), each experiment was repeated multiple times in order to assess reproducibility of the results (Table 1). Also, for a given boundary condition and at each shear velocity, we analyzed 50+ stick-slip events and report the mean value and statistical variability with error bars calculated by using a standard error of the mean (SEM) method.

3. Results

3.1. Anatomy of a Laboratory Stick-Slip Event

Experiments were conducted using a computer-controlled displacement history. Shearing began with an initial phase at 10 μm/s for ~6 mm (shear strain of 2–3), which served to condition the layers, localize shear, and establish a steady state value of sliding friction (Figure 3a). Upon initial loading, shear stress (τ) increased linearly to an inelastic yield point, after which stick-slip instabilities began and the maximum

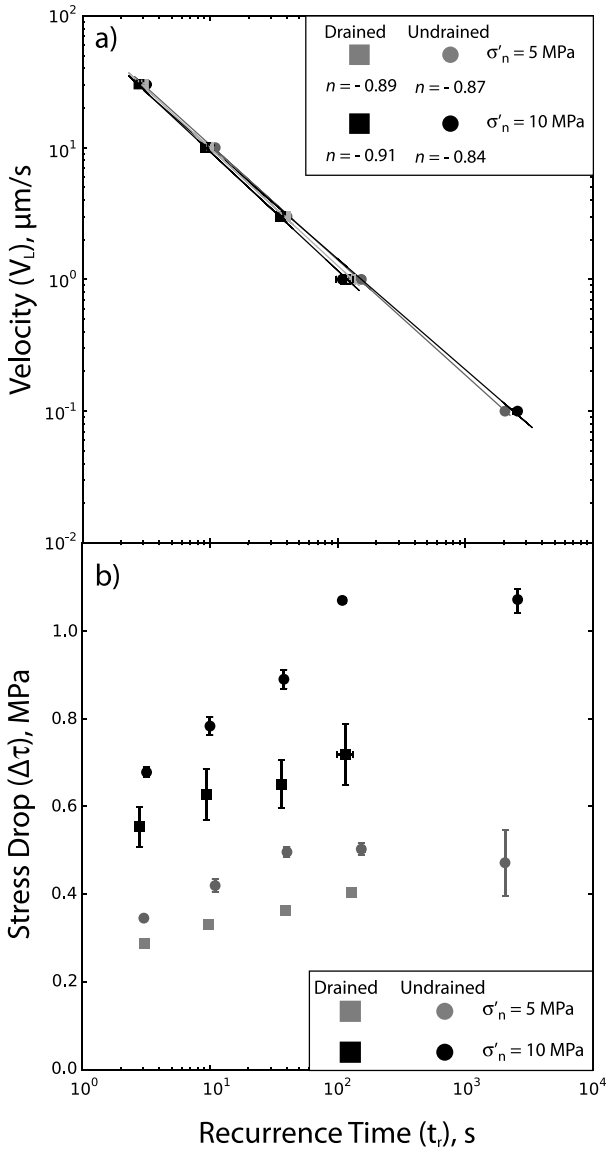

Figure 5. (a) Loading velocity (V_L) versus recurrence time (t_r) for experiments under drained and undrained boundary conditions at effective normal stresses of 5 and 10 MPa. Data are fit with a least squares polynominal fit with residual error ($R^2 < 0.99$). (b) Evolution of stress drop ($\Delta\tau$ as a function of recurrence time for all the experiments at effective normal stress of 5 and 10 MPa, under drained (square) and undrained (circles) boundary conditions.

(τ_{max}) and minimum (τ_{min}) stresses reached steady state values. We then imposed a series of velocity step tests (Figure 3), from 0.1 to 1 μm/s or 1 to 30 μm/s to measure the rate and state dependence of friction (Table 1).

Laboratory stick-slip events can be described by a typical three stage loading history (Figure 4). Initially, shear stress increases linearly with shear displacement, during elastic loading, characterized by stiffness k, which we cast as shear stress per shear displacement, MPa/μm (Figure 4a). During this stage, layer thickness (h) is essentially constant, consistent with elastic deformation at granular contacts. Deviation from the linear-elastic behavior marks the onset of plastic strain and aseismic creep. At this point gouge layers begin to dilate (Figure 4b), consistent with elasto-plastic deformation at grain contacts and granular rearrangement. [*Anthony and Marone*, 2005; *Scuderi et al.*, 2014]. We define preseismic slip as the shear displacement that occurs after elastic loading and prior to failure. For undrained loading, dilation occurs during preseismic slip and pore fluid pressure decreases, causing an overall increase of the effective normal stress (Figure 4c). Stick-slip failure begins at τ_{max}, and dynamic slip causes an abrupt stress drop (to a residual value, τ_{min}), abrupt compaction, and an increase in pore fluid pressure (Figure 4).

Consistent with previous studies, we observe that stress drop ($\Delta\tau = \tau_{max} - \tau_{min}$), interevent recurrence time (t_r), and layer thickness (h) vary systematically with shear velocity (Figures 3b and 3c and S1a and S1b) [*Mair et al.*, 2002; *Anthony and Marone*, 2005; *Savage and Marone*, 2007; *Scuderi et al.*, 2014; *Leeman et al.*, 2014; *Beeler et al.*, 2014]. We find that for an increase in velocity, the magnitude of stress drop decreases (Figure 3b, left) and the frequency of events increases (i.e., interevent time decreases) (Figure 3b, right). Gouge layer thickness (h) also shows a strong dependence on shear velocity (Figure 3c, left). Due to our sample geometry, layers undergo geometrical thinning with shear. In order to accurately determine variations in layer thickness associated with each stick-slip event, we corrected layer thickness data for layer thinning by removing the linear trend for thinning (Figure 3c, right) [*Scott et al.*, 1994; *Samuelson et al.*, 2009]. Note that for a series of stick-slip events at a given shear velocity, the preseismic dilation and coseismic compaction are equal and the net gouge porosity does not vary with displacement. For higher shear velocity, stress drop, stick-slip recurrence interval, and dilation/compaction decrease.

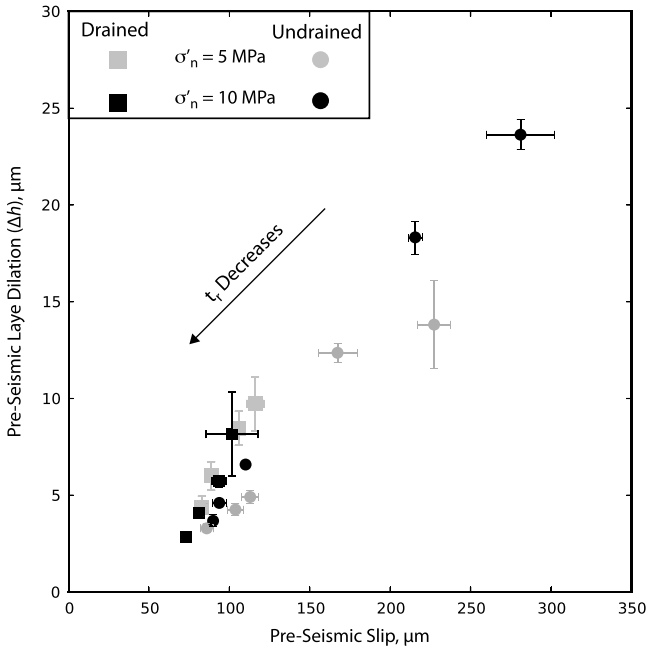

Figure 6. Evolution of preseismic layer dilation (Δh) as a function of preseismic slip for experiments performed at $\sigma'_n = 5$ and 10 MPa, under drained and undrained boundary conditions.

3.2. Stick-Slip Stress Drop

Loading velocity (V_L) has a systematic control on stick-slip stress drop and interevent recurrence time (t_r), that can be described as

$$V_L = C\ t_r^{\,n} \tag{3}$$

where C is a scaling constant and n is the power law exponent, consistent with previous work [*Karner and Marone*, 2000; *Beeler et al.*, 2001b]. For our experiments n is −0.87 (undrained) and −0.89 (drained) for $\sigma'_n = 5$ MPa, and $n = -0.84$ (undrained) and −0.91 (drained) at $\sigma'_n = 10$ MPa (Figure 5a). Equation (3) indicates that the slower the imposed shear velocity, the longer the resultant recurrence time between events. Although, the difference of n between the drained and undrained cases at $\sigma'_n = 5$ MPa is very small, we also find consistent differences at $\sigma'_n = 10$ MPa.

For undrained boundary conditions, we observe that stress drop increases with increasing recurrence time and effective normal stress (Figure 5b). Parameter $\Delta\tau$ is smaller at $\sigma'_n = 5$ MPa (0.2 MPa $< \Delta\tau <$ 0.5 MPa) compared to $\sigma'_n = 10$ MPa case, where 0.4 $< \Delta\tau <$ 1.1 MPa. For a given effective normal stress, the evolution of stress drop with recurrence time shows a log linear character up to about 100 s and is then flat for higher values of t_r. Stress drop is greatest for the longest recurrence times (i.e., slowest shear velocities). For t_r below 100 s (corresponding to shear velocity of ~3 μm/s) stress drop varies by ~ 0.13 MPa/decade at $\sigma'_n = 5$ MPa and 0.23 MPa/decade at $\sigma'_n = 10$ MPa.

For drained boundary conditions, we find the same general relationship between stress drop and recurrence time; however, stress drops are smaller than for undrained conditions. Stress drop decreases log linearly with decreasing recurrence time at a rate of 0.07 MPa/decade at $\sigma'_n = 5$ MPa and 0.09 MPa/decade when $\sigma'_n = 10$ MPa, a decrease of a factor of 1.2 and 1.4, respectively, when compared with undrained behavior. In general, we report that stick-slip stress drop and recurrence time are influenced by the fluid boundary condition. We observe that under undrained loading the recurrence time is longer and the stress drop is bigger compared with drained conditions.

3.3. Gouge Dilation and the Evolution of Pore Fluid Pressure During Preseismic Creep

We report high-resolution measurements of layer dilation/compaction during stick-slip in order to assess time-dependent deformation and associated changes of pore pressure. We observe that the preseismic layer dilation (Δh) evolves accordingly with the amount of preseismic slip and varies as a function of recurrence time (t_r), hydrological boundary conditions and effective normal stress (Figure 6). In general, gouge deformed under undrained boundary conditions always show larger dilation and longer preseismic slip when compared with the drained case. In all cases, preseismic slip and gouge dilation increase with increasing recurrence time, likely due to time-dependent processes at grain-to-grain contacts. For drained boundary conditions, gouge dilation is larger and preseismic slip is longer when the gouge is deformed at $\sigma'_n = 5$ MPa. The opposite is true under undrained boundary conditions, with gouge deformed at $\sigma'_n = 10$ MPa showing a larger dilation and longer preseismic slip than the $\sigma'_n = 5$ MPa case.

Our data show that the magnitude of preseismic dilation and pore fluid depressurization is controlled by the effective normal stress and scales directly with the magnitude of the stress drop (Figures 7, 8, 9 and 10c). In Figure 7 we report typical curves for shear stress, layer thickness, and pore fluid pressure at a constant shear

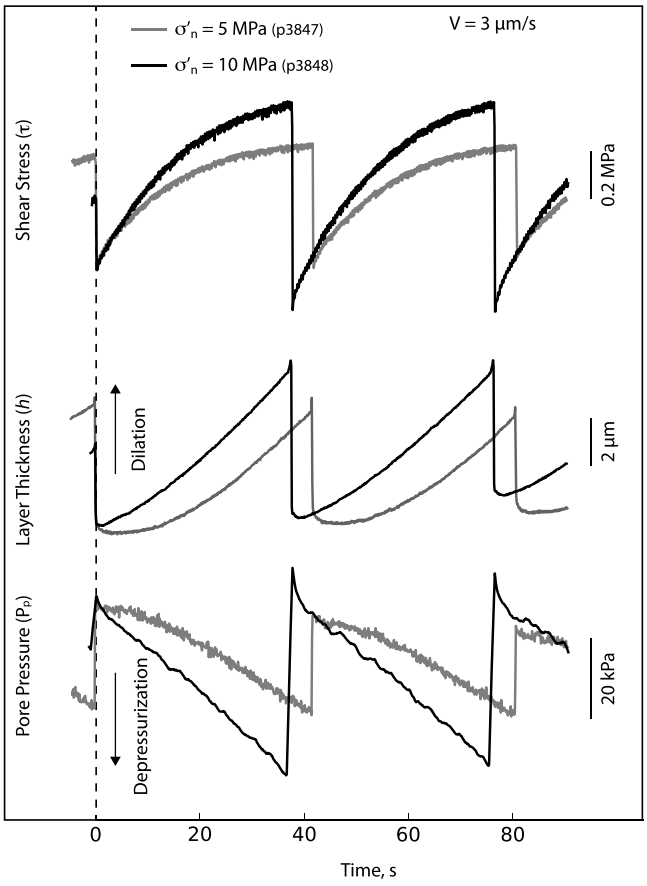

Figure 7. Details of shear stress (τ), gouge layer thickness (h), and pore fluid pressure (P_p) as a function of time for a section of experiments at a constant shear velocity of 3 μm/s. We show experiment conducted under undrained boundary conditions at $\sigma'_n = 5$ MPa (gray), and $\sigma'_n = 10$ MPa (black).

velocity of 3 μm/s for gouges deformed at $\sigma'_n = 5$ and 10 MPa. Gouge deformed at $\sigma'_n = 5$ MPa is characterized by an initial stage of constant layer thickness, suggesting elastic deformation at granular contacts. As the stress builds and deviates from linear-elastic behavior, layers begin to dilate and pore fluid pressure decreases until dynamic failure and the cycle repeats. Conversely, when gouge is deformed at $\sigma'_n = 10$ MPa, we document a significant increase in gouge dilation directly related to a larger pore fluid depressurization (Figure 7). Details of typical curves for single stick-slip events are reported in Figure 8 for a constant σ'_n of 5 MPa and different velocities (0.1 and 1 μm/s), and in Figure 9 for different effective normal stresses (5 and 10 MPa) and at a constant velocity (0.1 μm/s). Stick-slip characteristics are modulated by the shear velocity, with the shear strength and preseismic slip decreasing accordingly with t_r (i.e., increase shear velocity) (Figure 8a). During aseismic creep, layers dilate (Figure 8b), and pore pressure decreases (Figure 8c), both showing a nonlinear relationship with the shear stress, once a maximum threshold of τ is reached. On the other hand, we observe a linear relationship between pore fluid depressurization and layer dilation; the longer the gouge layers are under quasi-stationary contact the more they dilate during reshear, with larger pore fluid depressurization (Figure 8d). For a given shear velocity, the effective normal stress controls the magnitude of shear strength, with the pore fluid depressurization and layer dilation increasing as σ'_n is increased (Figure 9). We note that the characteristic trends described above for the evolution of τ, P_p, and h do not change as a function of σ'_n (Figure 9).

In general, when the preseismic pore fluid depressurization (ΔP_p) is plotted as a function of gouge layer dilation (Δh) for our range of loading rates, the data for $\sigma'_n = 10$ MPa always show a larger Δh and ΔP_p compared to those for $\sigma'_n = 5$ MPa (Figure 10a). For a given effective normal stress, the amount of preseismic dilation and pore fluid depressurization are controlled by the loading velocity (i.e., recurrence time), with the largest amount of Δh and ΔP_p occurring at the slowest velocities. As shear velocity is increased both dilation and pore fluid depressurization decrease accordingly (Figure 10a). A similar relationship is observed between the preseismic slip and ΔP_p, with the gouge that is deformed at $\sigma'_n = 10$ MPa, showing the greatest amount of preseismic slip, associated with the largest pore fluid depressurization, for the longest recurrence times (Figure 10b).

3.4. Post-Shear Contact Morphology

At the end of each experiment, gouge layers were collected for SEM analysis. In the following we report visual qualitative analysis, based on the observation of 50+ grain contacts for each boundary condition. A quantitative systematic analysis was impractical to perform due to the random orientation of the glass beads. Grain contact area and morphology depend strongly on the applied effective normal stress (Figures 11 and 12 and S2 and S3). Figure 11 shows detailed images of representative postexperiment

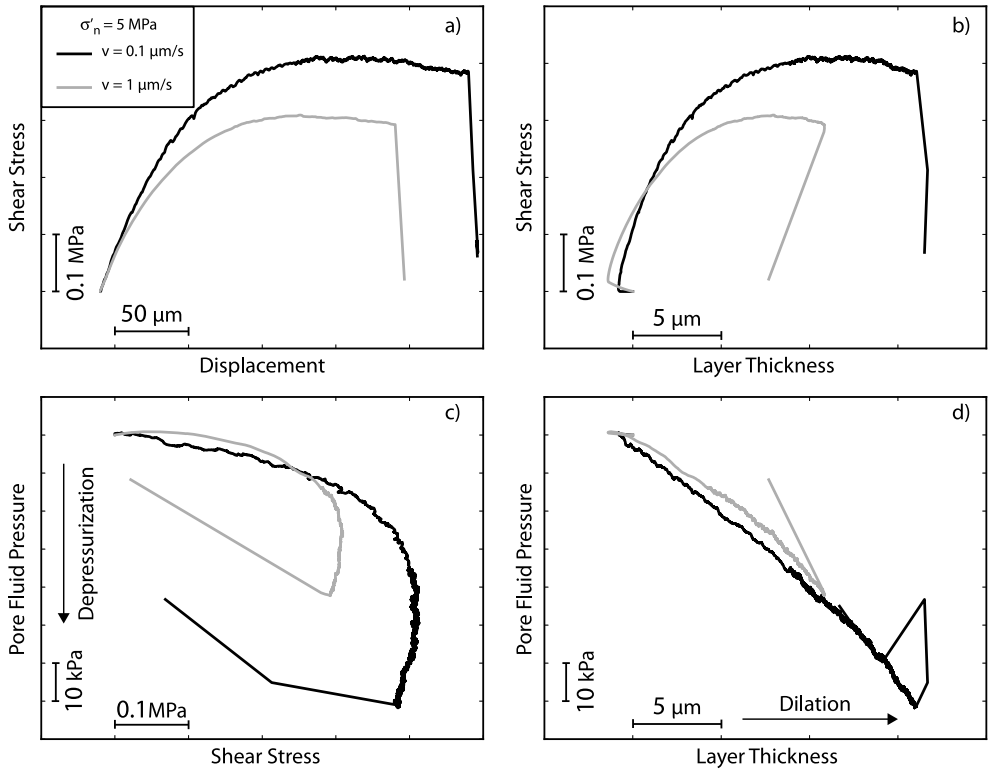

Figure 8. Details for two stick-slip events at $\sigma'_n = 5$ MPa and shear velocities of 0.1 (p4222) and 1 μm/s (p3847). (a) Shear stress increases linearly with displacement during elastic loading. Deviation from this relation marks the onset of aseismic creep. (b) Gouge layers dilate during elastic loading as shear stress builds up. During aseismic creep, shear strength reaches a constant value, with layers that continue to dilate, until coseismic compaction. (c) Pore fluid pressure decreases linearly as shear stress builds up during the elastic loading stage. During aseismic creep, we observe continuous depressurization. (d) Pore fluid pressure decreases linearly as the gouge layer dilates during the whole stick-slip cycle. An increase in shear velocity causes the relationships described above to decrease.

grains along with particle size data for experiments performed at effective normal stress of 5 MPa (Figure S2). Note that grains do not show evidence of bulk comminution, consistent with expectations for 5 MPa (Figure 11a). Particle sizes reveal a postexperiment d50 of 120 ± 2 μm, comparable with the d50 = 124 ± 1 μm of the starting material (Figure 11f). Grain contact deformation areas are roughly hemispherical in shape with diameter of 30 to 40 μm, depth of a few micrometer, and a well-defined outer rim (Figures 11b and 11c). Contact indentations show a well-developed system of striations that document slip from the edge of the contact toward the center (Figures 11b and 11c). Antithetic to the striations, we observe fractured zones (Figures 11b, 11d, and 11e) and the presence of fine-grained material (Figures 11d and 11e).

For experiments at 10 MPa effective normal stress grains are more fractured and contact deformation areas are more complex than at 5 MPa (Figures 12 and S3). Grain size is still representative of the undeformed material, with the majority of the grains still spherical (Figure 12a). Particle size analysis shows a d50 of 113 ± 2 μm, which is slightly smaller than the starting material (Figure 12f). Smaller grains also increase in abundance, with d10 going from 106 μm in the starting material to 22 ± 1 μm after shear (i.e., d10 represent the size of particles of which 10% of the sample is below the reported size). This represents the finer particles shown in Figure 12a that are formed due to spalling and grain fracture. Grain contact deformation areas are more elliptical in shape for experiments at 10 MPa, compared to those for 5 MPa, with a well-defined outer rim and a diameter of ~100 to 120 μm (Figures 12c and 12e). Striations develop from the outer rim and extend toward the center (Figures 12b and 12e). Normal to the striations, there are highly fractured areas, which extend on one side of the contact, forming a bulb-like shape, where finer particles (of size comparable with the d10 reported above) are present (Figures 12c and 12e). Unfortunately, we cannot assess variations in grain size and contact deformation as a function of loading velocity, which would require a series of constant velocity experiments.

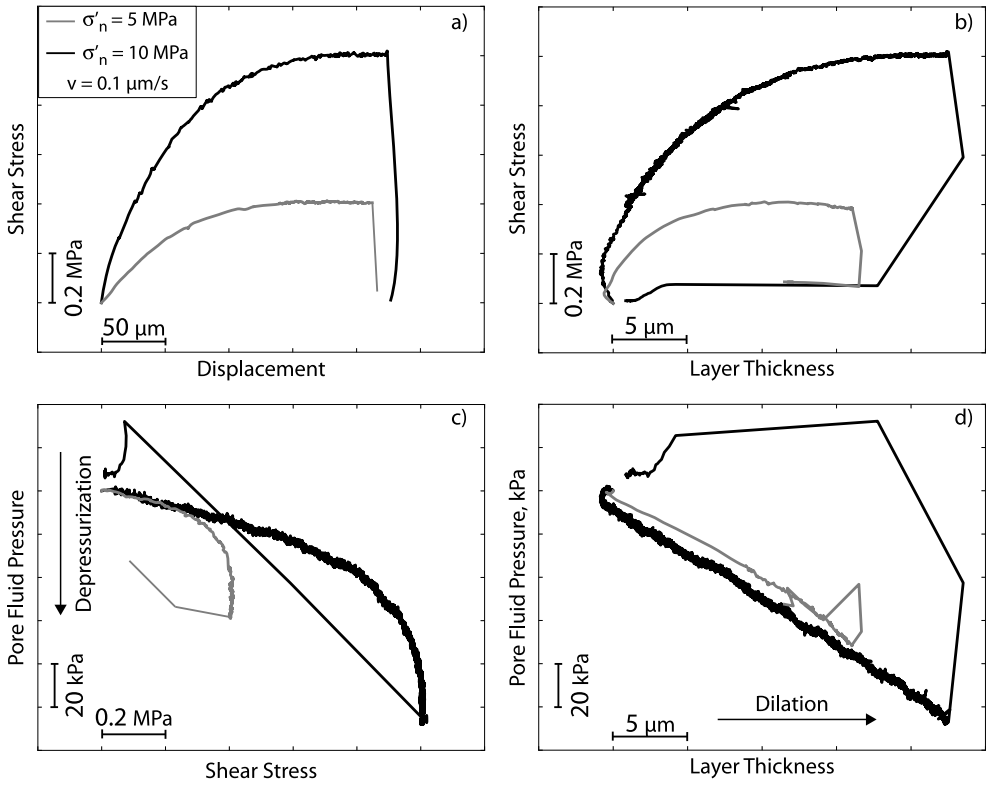

Figure 9. Details for two stick-slip events at $\sigma'_n = 5$ MPa (gray) (p4222) and 10 MPa (black) (p4223) under undrained conditions. (a) Shear stress increases linearly with displacement during elastic loading. Deviation from this relation marks the onset of aseismic creep. (b) Gouge layers dilate during elastic loading as shear stress builds up. During aseismic creep, shear strength reaches a constant value, with layers that continue to dilate, until co seismic compaction. (c) Pore fluid pressure decreases linearly as shear stress builds up during the elastic loading stage. During aseismic creep, we observe continuous depressurization. (d) Pore fluid pressure decreases linearly as the gouge layer dilates during the whole stick-slip cycle. An increase in effective normal stress causes the shear strength, preseismic slip, layer dilation, and pore fluid depressurization to all increase.

4. Discussion

4.1. Time-Dependent Strengthening and Its Effect on Dynamic Stress Drop

We find that loading rate (V_L) has a key affect on the recurrence time (t_r) of stick-slip events, showing an inverse power law relationship (Figure 5). Seismological observations, as well as experimental studies, have shown that this type of relationship can be applied to a variety of natural seismic sequences and laboratory data [e.g., *Marone et al.*, 1995; *Karner and Marone*, 2000; *Beeler et al.*, 2001a, 2014]. The exponent n in equation (3) reveals details of a fault's time-dependent strengthening [*Beeler et al.*, 2001b]. When $n = -1$, a one to one relationship between recurrence time and loading velocity is observed, which implies constant stress drop and no time-dependent frictional strengthening. In cases of appreciable time-dependent strengthening, the exponent n is expected to be > -1.0. Our results show that n is always larger than -1.0, implying that during the interseismic stage of stick-slip sliding, gouge layers undergo time-dependent strengthening, modulated by the effective normal stress and hydrological boundary conditions (Figure 5). Under undrained boundary conditions, we observe that n decreases from -0.87 to -0.84 when σ'_n is increased from 5 to 10 MPa. This implies that the degree of time-dependent strengthening increases as the effective stress is increased.

For a given normal stress, we observe that under drained conditions n is always closer to -1 when compared to undrained conditions. This is consistent with slightly higher effective normal stress for undrained boundary conditions, due to pore fluid pressure variations, which could enhance time-dependent strengthening. Similarly, when stress drop is plotted as a function of recurrence time for a given effective normal stress, we find that drained boundary conditions yield smaller stress drop compared to undrained conditions.

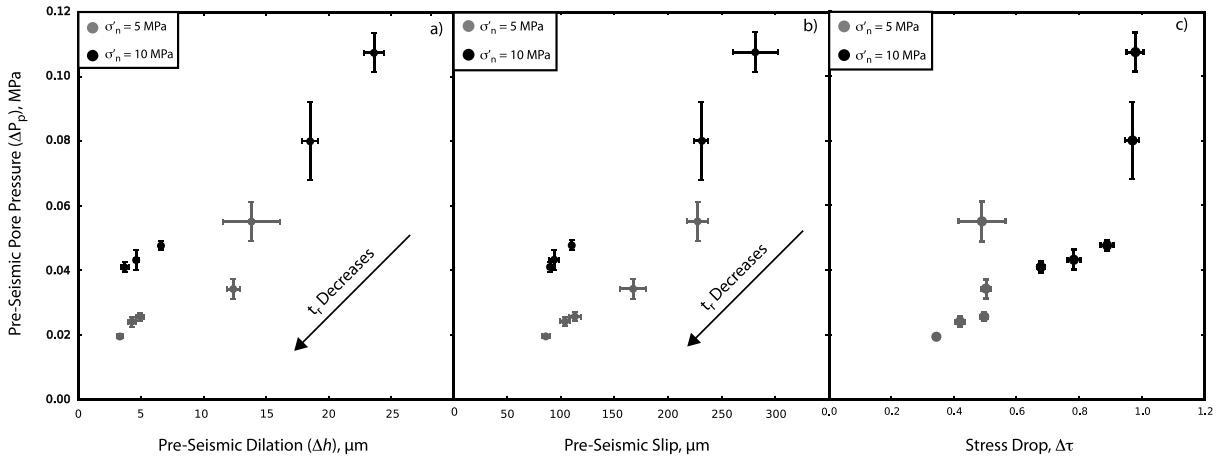

Figure 10. Evolution of the preseismic pore fluid depressurization as a function of (a) preseismic layer dilation and (b) preseismic slip for experiments conducted at $\sigma'_n = 5$ and 10 MPa.

This difference is more evident at $\sigma'_n = 10$ MPa (Figures 5 and S1b). Moreover, for a given hydrological boundary condition (i.e., drained or undrained), the gouge deformed at 10 MPa show a larger stress drop than the 5 MPa case (Figures 5, 7, and 9a). A combination of mechanical (i.e., dilation hardening associated with changes in pore fluid pressure) and chemical processes can control granular deformation at grain contact junctions within gouge layers. We observe that as the recurrence time increases (i.e., velocity is decreased), time-dependent strengthening during quasi-stationary contact and aseismic creep increases, causing larger dynamic stress drop until a threshold for $t_r > 100$ s, where the stress drop attains constant values (Figures 5b and S1). The threshold of 100 s could represent the lower limit of local normal stress needed for contact growth, or it could represent a fluid diffusion limit associated with contacts reaching a critical size.

4.2. Growth of Granular Contact Junctions

SEM postexperiment observations of ~50+ grains at both loads reveal that granular contact deformation size increases as a function of effective normal stress. Contact junctions are characterized by (1) a well-developed system of striations propagating toward the center of the contact, which is consistent with slip induced wear and ploughing during creep (Figures 11c and 12e); (2) a central zone with no evidence for slip or deformation (Figures 11c, 11d, and 12e); and (3) a fractured area, normal to the direction of the striations. We observe signs of material redistribution, surface fracture, and the presence of finer particles (Figures 11d and 12d). Fine particles may be the signature of mass transfer from dissolution at the interfaces enhanced by chemical reactions, such as pressure solution, and/or produced by the microfractures observed at the contact tip (Figures 11d, 11e, and 12c). Unfortunately, due to the gold coating used for the SEM investigation, we cannot perform a chemical spot analysis EDS (electron stimulated desorption) in order to characterize the finer particles and so discern if pressure solution is active during aseismic creep.

A variety of mechanisms have been proposed for time-dependent growth of contact area at grain junctions, such as plastic deformation [*Griggs and Blacic*, 1965], contact neck growth and welding [*Hickman and Evans*, 1991; *Renard et al.*, 2012], and pressure solution creep [*Niemeijer et al.*, 2008, 2010; *Gratier et al.*, 2014]. Time-dependent growth of granular contacts causes the interparticle friction to increase, which is reflected in a higher shear strength [*Marone*, 1998; *Nakatani and Scholz*, 2004]. Stress-enhanced pressure solution creep, during aseismic creep, can act as a mechanism for time-dependent gouge strengthening, by increasing the contact area at grain junctions (Figures 11 and 12) [e.g., *Hickman et al.*, 1995; *Niemeijer et al.*, 2008]. We posit that during aseismic creep, increasing shear displacement causes interparticle rolling and plastic deformation, possibly enhanced by pressure solution (Figures 13a, C1, and 13b, C1). As a result, stress will increase at the edges of contacts in the shear direction (Figures 13a, C2, and 13b, C2). Microslips associated with microfractures at the tip of the contact junctions can further increase the contact area, promoting more aseismic creep until a favorable orientation for sliding (φ_f) is achieved and catastrophic failure occurs (Figures 13b and 13c) [*Morgan and Boettcher*, 1999; *Johnson et al.*, 2013; *Ferdowsi et al.*, 2013]. These processes are

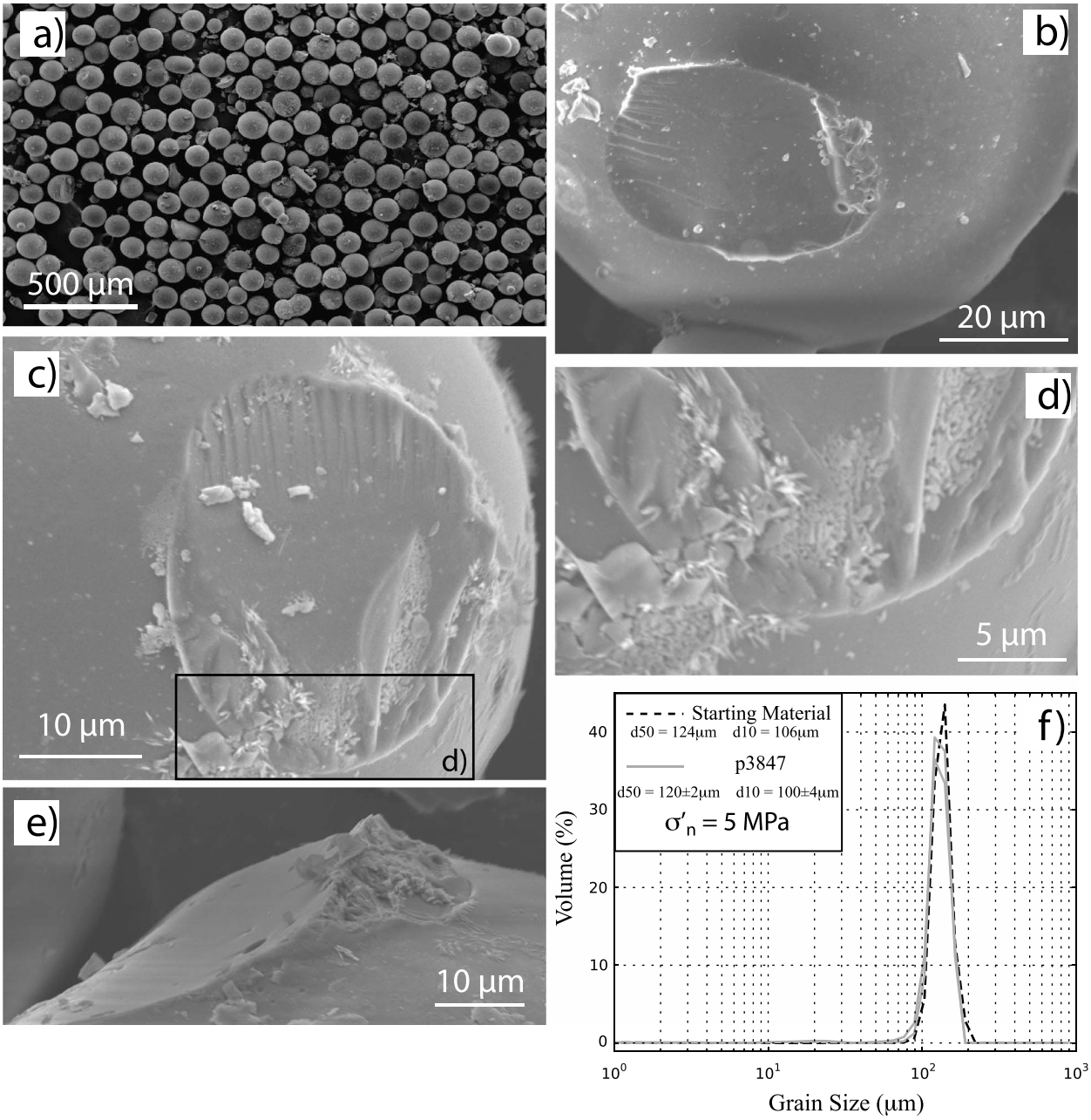

Figure 11. (a–e) Post experiment SEM images and (f) particle size distribution analysis of glass beads for experiments run at $\sigma'_n = 5$ MPa, under undrained boundary conditions, and at the noted magnification scale. Beads show little or no evidence of bulk crushing or comminution as confirmed by the particle size analysis (values of d50 and d10 represent the same quantities as reported in Figure 2) (Figure 11a). Details of grain-to-grain contact properties (Figures 11b–11e). Grain-to-grain contacts are characterized by a subrounded shape with a well-defined outer rim (Figures 11b and 11c). Striations are observed to propagate inward toward the contact (Figures 11b and 11c). Antithetic to the striations, we observe a fractured zone of probable stress concentration during shear (Figures 11d and 11e).

enhanced by higher normal stress consistent with our observations (Figures 13d and 13e) showing the following: (1) larger contact area; (2) evolution in contact shape, from subrounded (5 MPa) to elliptical-like shapes that expand in the direction of shear (10 MPa); and (3) a more mature system of fractures at $\sigma'_n = 10$ MPa. Furthermore, based on our mechanical data, which show an increase in time-dependent strengthening (Figure 5a), stress drop magnitude (Figure 5b) and larger dilation associated with longer preseismic slip (Figure 6) as a function of the hydrological boundary conditions, we posit that chemically activated creep is favored when the gouge layers are sheared under undrained conditions. We note that acoustic techniques (e.g., Figure 12c of *Johnson et al.* [2013]) document microslip precursors in sheared

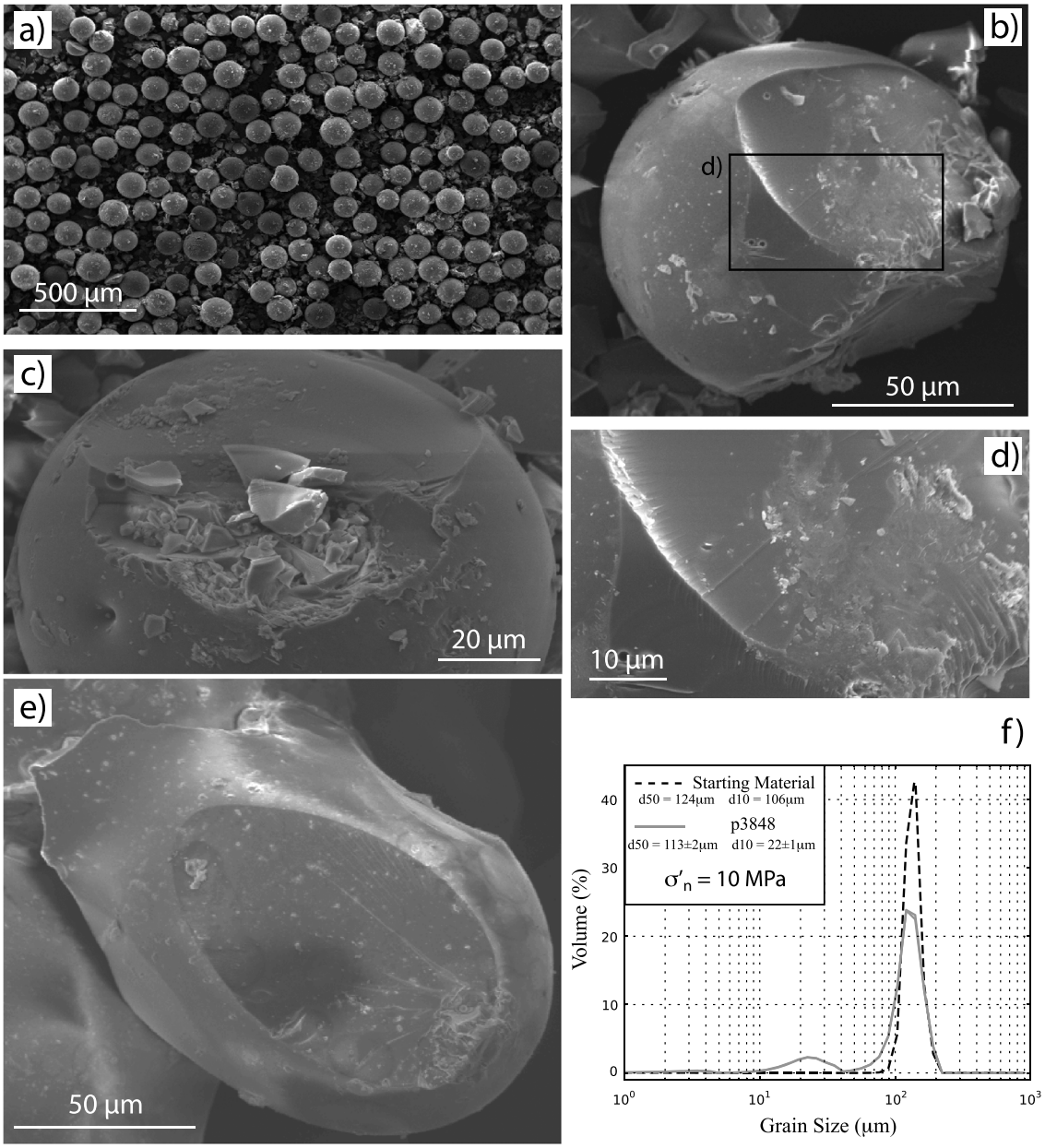

Figure 12. (a–e) Post experiment SEM images and (f) particle size distribution analysis of glass beads for experiments at $\sigma'_n = 10$ MPa, under undrained boundary conditions, and at the noted magnification scale. Beads show minor evidence of bulk crushing and comminution (Figure 12a). Particle grain size analyses (Figure 12f) reveals that the d50 is slightly smaller than for experiments at $\sigma'_n = 5$ MPa, and a significant decrease in the d10 to a value of ~23 µm. Details of contact junction properties (Figures 12b–12e). A symmetric contact geometry, probably due to two different cycles of stick-slip involving this bead (Figure 12b). Details shown in Figure 12d reveal the propagation of striations toward the center of the contact. The fractured zone observed in Figure 13e is wider and characterized by the formation of thinner particles corresponding to the finer particle size of d10 (Figure 12c). A top view of a grain-to-grain contact (Figure 12e). Note the elliptical-like shape characterized by a well-developed system of fractures on one end of the contact and fractures on the opposite side.

granular material well prior to stick-slip failure. This is consistent with increased grain movements (i.e., shearing and small rotations) when the material is fully dilated, just before failure occurs. Furthermore, digital elevation model (DEM) simulations [*Aharonov and Sparks*, 2004; *Ferdowsi et al.*, 2013; *Johnson et al.*, 2013] show that grain movement accelerates before failure. The combination of these results leads us to believe that microfractures could contribute to precursory activity. In summary, grain deformation is documented that intensifies with pressure. It is highly likely that it is responsible for the time dependent strengthening.

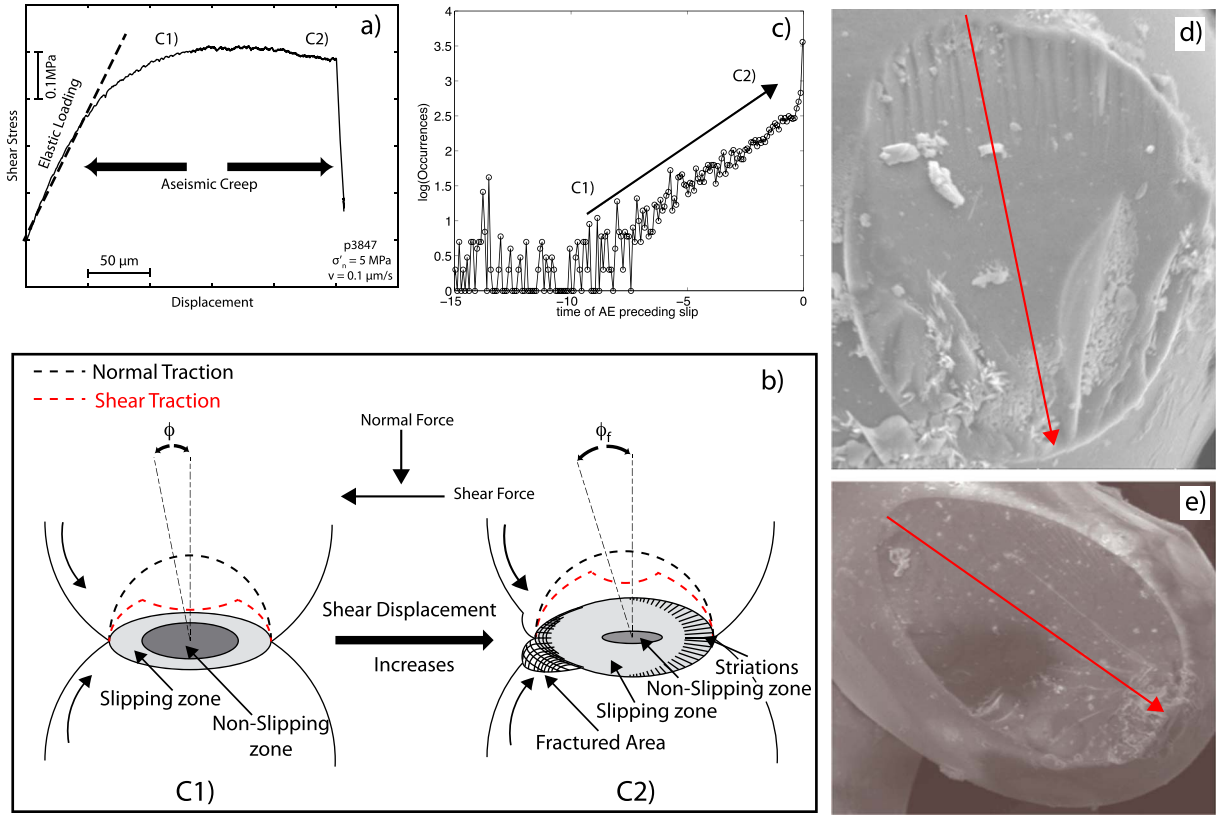

Figure 13. (a) Evolution of shear stress with displacement for a representative stick-slip event. The linear-elastic portion of loading and the subsequent aseismic creep are shown. (b) Schematic representation of grain-to-grain contact evolution under shear [modified after *Boitnott et al.*, 1992]. C1 and C2 represent the evolution of contact deformation as shear displacement is increased during aseismic creep for a single stick-slip cycle with ϕ in C1 representing the orientation of the force chains in respect to the shear direction and ϕ_f in C2 the critical orientation for failure. For reference we report C1 and C2 in Figures 13a and 13c. (c) PDF of acoustic emissions (AE) during a stick-slip event from *Johnson et al.* [2013]. The number of events is reported as a function of time. Note the exponential increase of AE when the gouge layers approach dynamic failure. (d, e) Grain-to-grain contacts reported in Figures 11c and 12e, respectively. The red arrows indicate the inferred sense of shear.

4.3. Influence of P_p and Δh on Preseismic Slip

We find that layer dilation and preseismic slip show a direct relationship with pore fluid depressurization. During the preseismic stage of stick-slip, both quantities increase as a function of recurrence time (Figures 10a and 10b). For a given effective normal stress, we document that the longer the gouge layers are under quasi-stationary contact (for slow loading rates), the larger the dilation, the longer the preseismic slip (Figure 6), and the larger the pore fluid depressurization (Figures 8, 9, and 10). We also observe that an increase in effective normal stress from 5 to 10 MPa causes Δh, preseismic slip, and pore fluid depressurization to increase (Figures 9 and 10). Details on single stick-slip cycles reveal that the pore fluid pressure decreases linearly with gouge layer dilation during the preseismic slip until failure occurs (Figures 8d and 9d), indicating a direct relationship between increase in porosity and gouge depressurization. On the other hand, we observe a nonlinear relationship between gouge depressurization and layer dilation with shear stress (Figures 8b and 8c and 9b and 9c), which is indicative that the feedback between micromechanical deformation (i.e., layer dilation) and fluid depressurization control the aseismic creep before failure. This relation is consistently observed at different shear velocities (Figure 8) and for both the effective normal stresses investigated (Figure 9). A strong contribution to gouge layer dilation during the stick portion of the stick-slip cycle is time-dependent, elasto-plastic deformation at grain contacts. It has been shown that under quasi-stationary contact, grain contact junctions grow with time due to physicochemical processes [e.g., *Rossi et al.*, 2007; *Renard et al.*, 2012; *Gratier et al.*, 2014]. A wider contact area increases the interparticle frictional resistance to shear, inducing more preseismic dilation. Our mechanical observations of time-dependent layer dilation and preseismic slip are in good agreement with the observed microstructures at grain contacts

and show that the more the gouge layer dilates, the longer the preseismic slip, consistent with increased area of grain-to-grain contacts.

For undrained loading, we posit that pore fluid depressurization, and the consequent increase in effective normal stress, can enhance stress at grains contacts, causing further contact area growth. A larger contact area increases time-dependent plastic deformation (i.e., aseismic creep), favoring time-dependent strengthening (Figure 5a). In this context a series of feedback processes between pore fluid depressurization and deformation at grain contacts, during aseismic creep, control the amount of preseismic slip, recurrence time, and the magnitude of dynamic stress drop by controlling the growth of contact area.

4.4. Implications for Fault Zones and Earthquake Prediction Models

Our observations provide important insights on the deformation mechanisms that dictate time-dependent phenomena at grain junctions within pressurized, fluid-rich granular material, at geophysical stress levels. Our observations, on glass spheres, indicate complex deformation patterns that are controlled by the applied stress field and highlight the role of hydrological boundary conditions (i.e., drained or undrained) on mechanical deformation. Although the material used in our experiments, silica glass beads, is simplified compared to fault rocks, the underlying deformation mechanisms may be similar in both cases. Because of the simple geometry of this system and high control on many parameters (i.e., particle shape and size), glass spheres are often used in DEM models and are considered as a first approximation to understand the complexity of the mechanisms that characterize real fault gouge during deformation. On the other hand, the simplicity and homogeneity of this system affect its mechanical behavior [i.e., *Mora and Place*, 1998; *Frye and Marone*, 2002; *Aharonov and Sparks*, 2004].

Laboratory stick-slip frictional sliding is often associated with shallow crustal earthquakes [*Brace and Byerlee*, 1966]. The dilatancy/fluid diffusion hypothesis, raised from seismological and laboratory observations, assumes fluid redistribution associated with stress dependent dilatancy and microcracks, during the seismic cycle [*Scholz et al.*, 1972; *Sibson*, 1994; *Hickman et al.*, 1995]. *Rubinstein et al.* [2012a, 2012b] analyzed laboratory earthquakes with the slip- and time-dependent model compared to the null hypothesis of constant slip and/or perfect periodicity. They found that such models do not improve the description of earthquake behavior, because they oversimplify very complex processes that control the evolution of fault gouge strength during the earthquake cycle.

Our experimental observations reveal that time- and stress-dependent dilatancy, associated with variations in pore fluid pressure, under undrained conditions, enhance time-dependent strengthening and increase stress drop magnitude. Pressure solution creep may play a fundamental role in controlling aseismic creep and thus the recurrence time of faulting events. In this context, hydrological boundary conditions and temperature variations associated with stress-dependent micromechanical processes must be taken in account when formulating models for earthquake prediction, because they can strongly control the evolution of shear strength, recurrence time, and dynamic stress drop.

5. Summary

We present detailed observations of poromechanical properties of sheared granular layers undergoing stick-slip frictional sliding. Our data show that time-dependent frictional strengthening and stick-slip stress drop magnitude scale with effective normal stress and depend on hydrological boundaries conditions. When gouge layers are deformed under undrained boundary conditions, time-dependent strengthening and the magnitude of stress drop are larger than for with drained conditions. We observed that under undrained conditions, the amount of gouge layer dilation, pore fluid depressurization, and pre seismic-slip are all directly related, increasing as a function of effective normal stress and decreasing as a function of stick-slip recurrence time. Postexperiment SEM observations reveal that granular contact area increases as a function of effective normal stress, and its evolution is likely controlled by pressure solution creep. We propose that under undrained conditions, a series of feedback processes between pore fluid depressurization and pressure solution creep control time-dependent elasto-plastic deformation at contact junctions. As a result, the longer a gouge layer is under quasi-stationary contact, the more the layer dilates upon reshear and the larger the drop in pore fluid pressure. Both of these quantities are controlled by the evolution of contact junctions, resulting in more time-dependent strengthening and larger stress drops than under drained conditions. Our observations have important implications for earthquake prediction models and theoretical models of granular deformation.

Acknowledgments
This work was funded by institutional support at the Los Alamos National Laboratory, through a grant from the Institute of Geophysics and Planetary Physics and NSF grants EAR1045825 and EAR1215856 to C.M. We thank D. Elsworth for helpful scientific discussions and S. Swavely for the technical support. We also thank three anonymous reviewers whose comments helped improve this manuscript. Our data are available by FTP transfer by contacting the corresponding author.

References

Aharonov, E., and D. Sparks (2004), Stick-slip motion in simulated granular layers, *J. Geophys. Res.*, *109*, B09306, doi:10.1029/2003JB002597.

Andrews, D. J. (2002), A fault constitutive relation accounting for thermal pressurization of pore fluid, *J. Geophys. Res.*, *107*(B12), 2363, doi:10.1029/2002JB001942.

Anthony, J. L., and C. Marone (2005), Influence of particle characteristics on granular friction, *J. Geophys. Res.*, *110*, B08409, doi:10.1029/2004JB003399.

Audet, P., M. G. Bostock, N. I. Christensen, and S. M. Peacock (2009), Seismic evidence for overpressured subducted oceanic crust and megathrust fault sealing, *Nature*, *457*(7225), 76–78, doi:10.1038/nature07650.

Beeler, N. M., D. Lockner, and S. Hickman (2001a), A simple stick-slip and creep-slip model for repeating earthquakes and its implication for microearthquakes at Parkfield, *Bull. Seismol. Soc. Am.*, *91*, 1797–1804, doi:10.1785/0120000096.

Beeler, N. M., S. H. Hickman, and T. F. Wong (2001b), Earthquake stress drop and laboratory-inferred interseismic strength recovery, *J. Geophys. Res.*, *106*, 30,701–30,713, doi:10.1029/2000JB900242.

Beeler, N. M., T. Tullis, J. Junger, B. Kilgore, and D. Goldsby (2014), Laboratory constraints on models of earthquake recurrence, *J. Geophys. Res. Solid Earth*, *119*, 8770–8791, doi:10.1002/2014JB011184.

Bizzarri, A., and M. Cocco (2006), Correction to "A thermal pressurization model for the spontaneous dynamic rupture propagation on a three-dimensional fault: 1. Methodological approach", *J. Geophys. Res.*, *111*, B11302, doi:10.1029/2006JB004759.

Boitnott, G., R. Biegel, C. H. Scholz, N. Yoshioka, and W. Wang (1992), Micromechanics of rock friction 2: Quantitative modeling of initial friction with contact theory, *J. Geophys. Res.*, *97*, 8965–8978, doi:10.1029/92JB00019.

Bos, B., and C. J. Spiers (2002), Fluid-assisted healing processes in gouge-bearing faults: Insights from experiments on a rock analogue system, *Pure Appl. Geophys.*, *159*(11-12), 2537–2566, doi:10.1007/s00024-002-8747-2.

Brace, W., and J. Byerlee (1966), Stick-slip as a mechanism for earthquakes, *Science*, *153*(3739), 990–992.

Chester, F. (1995), A rheologic model for wet crust applied to strike slip faults, *J. Geophys. Res.*, *100*, 33–44.

Chester, F., and N. Higgs (1992), Multimechanism friction constitutive model for ultrafine quartz gouge at hypocentral conditions, *J. Geophys. Res.*, *97*, 1859–1870, doi:10.1029/91JB02349.

Dieterich, J. H., and B. D. Kilgore (1994), Direct observation of frictional contacts: New insights for state-dependent properties, *Pure Appl. Geophys.*, *143*(1-3), 283–302, doi:10.1007/BF00874332.

Ferdowsi, B., M. Griffa, R. A. Guyer, P. A. Johnson, C. Marone, and J. Carmeliet (2013), Microslips as precursors of large slip events in the stick-slip dynamics of sheared granular layers: A discrete element model analysis, *Geophys. Res. Lett.*, *40*, 4194–4198, doi:10.1002/grl.50813.

Ferdowsi, B., M. Griffa, R. A. Guyer, P. A. Johnson, and J. Carmeliet (2014a), Effect of boundary vibration on the frictional behavior of a dense sheared granular layer, *Acta Mech.*, *225*(8), 2227–2237, doi:10.1007/s00707-014-1136-y.

Ferdowsi, B., M. Griffa, R. A. Guyer, P. A. Johnson, C. Marone, and J. Carmeliet (2014b), Three-dimensional discrete element modeling of triggered slip in sheared granular media, *Phys. Rev. E: Stat., Nonlinear, Soft Matter Phys.*, *89*(4), 042204, doi:10.1103/PhysRevE.89.042204.

Frye, K. M., and C. Marone (2002), Effect of humidity on granular friction at room temperature, *J. Geophys. Res.*, *107*(B11), 2309, doi:10.1029/2001JB000654.

Garagash, D. I., and L. N. Germanovich (2012), Nucleation and arrest of dynamic slip on a pressurized fault, *J. Geophys. Res.*, *117*, B10310, doi:10.1029/2012JB009209.

Goren, L., E. Aharonov, D. Sparks, and R. Toussaint (2011), The mechanical coupling of fluid-filled granular material under shear, *Pure Appl. Geophys.*, *168*(12), 2289–2323, doi:10.1007/s00024-011-0320-4.

Gratier, J., F. Renard, and B. Vial (2014), Postseismic pressure solution creep: Evidence and time-dependent change from dynamic indenting experiments, *J. Geophys. Res. Solid Earth*, *119*, 2764–2779, doi:10.1002/2013JB010768.

Griggs, D. T., and J. D. Blacic (1965), Quartz: Anomalous weakness of synthetic crystals, *Science*, *147*(3655), 292–295.

Hasegawa, A., K. Yoshida, and T. Okada (2011), Nearly complete stress drop in the 2011 M w 9.0 off the Pacific coast of Tohoku earthquake, *Earth Planets Space*, *63*(7), 703–707, doi:10.5047/eps.2011.06.007.

Hickman, S., R. Sibson, and R. Bruhn (1995), Introduction to special section: Mechanical involvement of fluids in faulting, *J. Geophys. Res.*, *100*(B7), 12,831–12,840, doi:10.1029/95JB01121.

Hickman, S. H., and B. Evans (1991), Experimental pressure solution in halite: The effect boundary structure of grain/interphase, *J. Geol. Soc.*, *148*, 549–560.

Hickman, S. H., and B. Evans (1992), *Fault Mechanics and Transport Properties of Rocks*, vol. 51, Academic Press.

Hirono, T., and Y. Hamada (2010), Specific heat capacity and thermal diffusivity and their temperature dependencies in a rock sample from adjacent to the Taiwan Chelungpu fault, *J. Geophys. Res.*, *115*, B05313, doi:10.1029/2009JB006816.

Hubbert, M., and W. Rubey (1959), Role of fluid pressure in mechanics of overthrust faulting, *Geol. Soc. Am. Bull.*, *70*, 115–166.

Johnson, P. A., H. Savage, M. Knuth, J. Gomberg, and C. Marone (2008), Effects of acoustic waves on stick-slip in granular media and implications for earthquakes, *Nature*, *451*(7174), 57–60, doi:10.1038/nature06440.

Johnson, P. A., B. Ferdowsi, B. M. Kaproth, M. Scuderi, M. Griffa, J. Carmeliet, R. A. Guyer, P.-Y. Le Bas, D. T. Trugman, and C. Marone (2013), Acoustic emission and microslip precursors to stick-slip failure in sheared granular material, *Geophys. Res. Lett.*, *40*, 5627–5631, doi:10.1002/2013GL057848.

Karner, S., and C. Marone (2000), Effects of loading rate and normal stress on stress drop and stick-slip recurrence interval, in *Geocomplexity and the Physics of Earthquakes*, *Geophys. Monogr. Ser.*, vol. 120, pp. 187–198, AGU, Washington, D. C.

Kitajima, H., and D. M. Saffer (2012), Elevated pore pressure and anomalously low stress in regions of low frequency earthquakes along the Nankai Trough subduction megathrust, *Geophys. Res. Lett.*, *39*, L23301, doi:10.1029/2012GL053793.

Leeman, J., M. Scuderi, C. Marone, D. M. Saffer, and T. Shinbrot (2014), On the origin and evolution of electrical signals during frictional stick slip in sheared granular material, *J. Geophys. Res. Solid Earth*, *119*, 4253–4268, doi:10.1002/2013JB010793.

Li, Q., T. E. Tullis, D. Goldsby, and R. W. Carpick (2011), Frictional ageing from interfacial bonding and the origins of rate and state friction, *Nature*, *480*(7376), 233–236, doi:10.1038/nature10589.

Mair, K., C. Marone, and K. M. Frye (2002), Influence of grain characteristics on the friction of granular shear zones, *J. Geophys. Res.*, *107*(B10), 2219, doi:10.1029/2001JB000516.

Marone, C. (1998), Laboratory-derived friction laws and their application to seismic faulting, *Annu. Rev. Earth Planet. Sci.*, *26*(1), 643–696, doi:10.1146/annurev.earth.26.1.643.

Marone, C., J. E. Vidale, and W. L. Ellsworth (1995), Fault healing inferred from time dependent variation in source properties of repeating earthquakes, *Geophys. Res. Lett.*, *22*, 3095–3098, doi:10.1029/95GL03076.

Mora, P., and D. Place (1998), Numerical simulation of earthquake faults with gouge: Toward a comprehensive explanation for the heat flow paradox, *J. Geophys. Res.*, *103*, 21,067–21,089, doi:10.1029/98JB01490.
Morgan, J., and M. Boettcher (1999), Numerical simulations of granular shear zones using the distinct element method: Shear zone kinematics and the micromechanics of localization, *J. Geophys. Res.*, *104*, 2703–2719, doi:10.1029/1998JB900056.
Nakatani, M., and C. H. Scholz (2004), Frictional healing of quartz gouge under hydrothermal conditions: 1. Experimental evidence for solution transfer healing mechanism, *J. Geophys. Res.*, *109*, B07201, doi:10.1029/2001JB001522.
Niemeijer, A., C. Marone, and D. Elsworth (2008), Healing of simulated fault gouges aided by pressure solution: Results from rock analogue experiments, *J. Geophys. Res.*, *113*, B04204, doi:10.1029/2007JB005376.
Niemeijer, A., C. Marone, and D. Elsworth (2010), Fabric induced weakness of tectonic faults, *Geophys. Res. Lett.*, *37*, L03304, doi:10.1029/2009GL041689.
Renard, F., S. Beauprêtre, C. Voisin, D. Zigone, T. Candela, D. K. Dysthe, and J.-P. Gratier (2012), Strength evolution of a reactive frictional interface is controlled by the dynamics of contacts and chemical effects, *Earth Planet. Sci. Lett.*, *341-344*, 20–34, doi:10.1016/j.epsl.2012.04.048.
Rossi, M., O. Vidal, B. Wunder, and F. Renard (2007), Influence of time, temperature, confining pressure and fluid content on the experimental compaction of spherical grains, *Tectonophysics*, *441*(1-4), 47–65, doi:10.1016/j.tecto.2007.05.001.
Rubinstein, J. L., W. L. Ellsworth, N. M. Beeler, B. D. Kilgore, D. A. Lockner, and H. M. Savage (2012a), Fixed recurrence and slip models better predict earthquake behavior than the time- and slip-predictable models: 2. Laboratory earthquakes, *J. Geophys. Res.*, *117*, B02307, doi:10.1029/2011JB008723.
Rubinstein, J. L., W. L. Ellsworth, K. H. Chen, and N. Uchida (2012b), Fixed recurrence and slip models better predict earthquake behavior than the time- and slip-predictable models: 1. Repeating earthquakes, *J. Geophys. Res.*, *117*, B02306, doi:10.1029/2011JB008724.
Rudnicki, J. (1984), Effects of dilatant hardening on the development of concentrated shear deformation in fissured rock masses, *J. Geophys. Res.*, *89*, 9259–9270, doi:10.1029/JB089iB11p09259.
Rudnicki, J., and J. Rice (1975), Conditions for the localization of deformation in pressure-sensitive dilatant materials, *J. Mech. Phys. Solids*, *23*(6), 371–394.
Samuelson, J., D. Elsworth, and C. Marone (2009), Shear-induced dilatancy of fluid-saturated faults: Experiment and theory, *J. Geophys. Res.*, *114*, B12404, doi:10.1029/2008JB006273.
Samuelson, J., D. Elsworth, and C. Marone (2011), Influence of dilatancy on the frictional constitutive behavior of a saturated fault zone under a variety of drainage conditions, *J. Geophys. Res.*, *116*, B10406, doi:10.1029/2011JB008556.
Savage, H. M., and C. Marone (2007), Effects of shear velocity oscillations on stick-slip behavior in laboratory experiments, *J. Geophys. Res.*, *112*, B02301, doi:10.1029/2005JB004238.
Savage, H. M., and C. Marone (2008), Potential for earthquake triggering from transient deformations, *J. Geophys. Res.*, *113*, B05302, doi:10.1029/2007JB005277.
Scholz, C., P. Molnar, and T. Johnson (1972), Detailed studies of frictional sliding of granite and implications for the earthquake mechanism, *J. Geophys. Res.*, *77*, 6392–6406, doi:10.1029/JB077i032p06392.
Scott, D., C. Marone, and C. Sammis (1994), The apparent friction of granular fault gouge in sheared layers, *J. Geophys. Res.*, *99*, 7231–7247, doi:10.1029/93JB03361.
Scuderi, M. M., A. R. Niemeijer, C. Collettini, and C. Marone (2013), Frictional properties and slip stability of active faults within carbonate–Evaporite sequences: The role of dolomite and anhydrite, *Earth Planet. Sci. Lett.*, *369–370*, 220–232, doi:10.1016/j.epsl.2013.03.024.
Scuderi, M. M., B. Carpenter, and C. Marone (2014), Physicochemical processes of frictional healing: Effects of water on stick-slip stress drop and friction of granular fault gouge, *J. Geophys. Res. Solid Earth*, *119*, 4090–4105, doi:10.1002/2013JB010641.
Segall, P., and S. Lu (2015), Injection-induced seismicity: Poroelastic and earthquake nucleation effects, *J. Geophys. Res. Solid Earth*, *120*, 1–22, doi:10.1002/2015JB012060.
Segall, P., and J. R. Rice (2006), Does shear heating of pore fluid contribute to earthquake nucleation?, *J. Geophys. Res.*, *111*, B09316, doi:10.1029/2005JB004129.
Segall, P., A. M. Rubin, A. M. Bradley, and J. R. Rice (2010), Dilatant strengthening as a mechanism for slow slip events, *J. Geophys. Res.*, *115*, B12305, doi:10.1029/2010JB007449.
Sibson, R. (1981), Controls on low-stress hydro-fracture dilatancy in thrust, wrench and normal fault terrains, *Nature*, *289*, 665–667.
Sibson, R. (1982), Fault zone models, heat flow, and the depth distribution of earthquakes in the continental crust of the united states, *Bull. Seismol. Soc. Am.*, *72*(1), 151–163.
Sibson, R. (1994), An assessment of field evidence for 'Byerlee' friction, *Pure Appl. Geophys.*, *142*(3), 645–662.
Sibson, R. H. (1992), Implications of fault-valve behaviour for rupture nucleation and recurrence, *Tectonophysics*, *211*(1–4), 283–293, doi:10.1016/0040-1951(92)90065-E.
Sleep, N., and M. Blanpied (1992), creep, compaction and the weak rheology of major faults, *Nature*, *359*, 687–692.
Sundaram, P., R. Goodman, and C. Wang (1976), Precursory and coseismic water-pressure variations in stick-slip experiments, *Geology*, *4*, 108–110.
Teufel, L. (1980), Precursive pore pressure changes associated with premonitory slip during stick-slip sliding, *Tectonophysics*, *69*, 189–199.
Verberne, B. A., J. H. P. de Bresser, A. R. Niemeijer, C. J. Spiers, D. A. M. de Winter, and O. Plumper (2013), Nanocrystalline slip zones in calcite fault gouge show intense crystallographic preferred orientation: Crystal plasticity at sub-seismic slip rates at 18-150 C, *Geology*, *41*(8), 863–866, doi:10.1130/G34279.1.
Weeks, J. D., N. M. Beeler, and T. E. Tullis (1991), Frictional behavior glass is like a rock, *Eos Trans. AGU*, *72*, 457–458, Fall Meeting Suppl.